Journal Pre-proof

Anatomy of a buried thrust belt activated during hydraulic fracturing

Naimeh Riazi, David W. Eaton

Please cite this article as: N. Riazi and D.W. Eaton, Anatomy of a buried thrust belt activated during hydraulic fracturing, *Tectonophysics* (2020), https://doi.org/10.1016/j.tecto.2020.22864

Anatomy of a buried thrust belt activated during hydraulic fracturing

Naimeh Riazi[1,*] nriazi@ucalgary.ca and David W. Eaton[1]

[1]Department of Geoscience, University of Calgary, Calgary, Alberta, Canada, T2N 1N4

[*]Corresponding author.

This file includes:

Main Text

Figs. 1-5

Abstract

Tectonically active fault networks are often inter-connected, but in the case of injection-induced seismicity, prior knowledge of fault architecture tends to be severely limited. In most cases, reactivated faults due to fluid injection are inferred, after-the-fact, by the spatial distribution of induced-seismicity hypocenters; such reliance on post-injection seismicity impedes any pre-operational risk analysis, as well as development of a more holistic understanding of fault-system models. By combining high-resolution, depth-migrated 3-D seismic data with a new focal-depth estimation method that reduces spatial uncertainty of hypocenters, this study pinpoints microearthquake fault activation within a buried thrust belt in the Montney Formation in western Canada (British Columbia). During hydraulic-fracturing operations, rupture nucleation occurred on seismically imaged thrust ramps that cut through the Debolt Formation, a massive carbonate layer that underlies the stimulated zone. High-resolution seismic images reveal transverse structures, interpreted as basement-controlled fold hinges or tear faults that transferred displacement between thrust faults during Late Cretaceous - Paleogene compressional shortening. The spatio-temporal pattern of induced seismicity suggests that these transverse structures provide permeable pathways for aseismic pore-pressure diffusion, thus connecting distinct thrust faults and enabling earthquake triggering on a timescale of days and at distances of up to 2 km from the injection wells. Inferred relationships highlight how the fault system is connected, including apparent stress concentrations at the intersections of transverse structures and orogen-parallel thrust ramps.

Keywords

Focal Induced seismicity, Fault imaging, Earthquake depth

Highlights

- High-resolution 3-D seismic data provides detailed imaging of a buried thrust system.
- Induced seismic events are accurately located using a novel method.
- Induced seismicity occurred above Precambrian basement.
- Imaged thrust ramps are connected by transverse structures.
- Transverse structures enable inter-fault pore-pressure communication (> 2 km).

1. Introduction

In nature, fault zones interact with each other at local and regional scales (Spotila and Anderson, 2004, Pondard et al., 2007) . As part of this interaction, earthquake fault systems exhibit dynamic behavior that leads to network-topology dependent nonlinear processes, characterized by power-law connectivity distributions and clustering in space and time (Rundle et al., 2001, Abe and Suzuki, 2006). Although most fault-system studies are focused on inter-plate fault systems, stress-interactions – including remotely triggered fluid diffusion – have been documented within intra-plate fault systems (e.g., Attanayake et al., 2019), demonstrating the potential applicability of these models to ancient fault systems in continental interiors. Moreover, in sedimentary basins, long-term fault interaction has been demonstrated to contribute to the creation of stratigraphic seals for conventional hydrocarbon reservoirs (Gray et al., 1999).

A surge of induced seismicity in continental-interior regions has occurred in parts of North America due to industrial activities linked to saltwater disposal and unconventional oil and gas extraction (Ellsworth, 2013, Eaton, 2018, Atkinson et al., 2020, Kettlety et al., 2019). In contrast to areas where saltwater disposal is the main triggering mechanism (e.g., Langenbruch and Zoback, 2017) hydraulic fracturing (injection of high-pressure fluids into tight rocks (Speight, 2016) is considered to be the main industrial driver of induced seismicity in western Canada (Bao and Eaton, 2016, Atkinson et al., 2016). To manage induced-seismicity risks arising from hydraulic fracturing and saltwater disposal, pre-operational risk management is desirable; however, there are a number of impediments, including: 1) a typical lack of publicly accessible high-resolution, depth-migrated 3-D seismic data that can provide detailed images of existing fault architecture, 2) a tendency within the industry to use seismic data for exploration rather than risk-management purposes, 3) a tendency for induced earthquakes to occur on previously unmapped faults (Alt and Zoback, 2017, Hennings et al., 2019). The latter tendency may be related, at least in some cases, to a lack of access to high-resolution seismic data or the subtle seismic expression of seismogenic structures (Eaton et al., 2018; Clarke et al. 2019).

Reliable and accurate seismic event locations can provide important clues regarding fault interaction and triggering mechanisms of induced earthquakes. However, event locations are subject to various sources of uncertainty (Riazi et al., 2020, Jones et al., 2014). For example, most earthquake location methods rely on an explicit model for wave velocities (Trugman and Shearer, 2017, Lomax, 2005, Zhang and Thurber, 2003, Waldhauser and Ellsworth, 2000), which may be insufficiently constrained by independent data. In the case of sensor networks deployed at the surface, focal depth is the least well resolved location parameter (Riazi et al., 2020); yet, accurate depth constraints are essential to quantify risk and to elucidate fault activation processes.

The objective of this study is to combine precise event locations of induced seismicity during hydraulic fracturing with high-resolution 3-D seismic images, in order to investigate fault-system behavior. This case study is located in the foreland of the northern Canadian Rocky Mountains, where relevant structural features include thrust faults with a flat-ramp geometry and fault-propagation folds, as well as transverse structures that connect distinct thrust sheets (Lebel et al., 1996). The complex architecture of the buried fault system is imaged by depth-migrated 3-D multicomponent seismic data, and subtle structural features are enhanced using seismic-attribute analysis. Robust and precise event hypocenters, with maximum magnitude of M_W 1.78, are obtained by combining a kinematic method for locating event epicenters with a recently developed method for focal-depth determination (Poulin et al., 2019) that leverages independent velocity information implicit in horizon correlations using P-P and P-S 3-D seismic images. The results demonstrate that during stimulation by fluid injection, fault-zone interaction can occur through transverse structures that provide pathways for fault activation at distances of up to 2 km from the injection wells.

2. Study area

This study is located near Fort St. John, British Columbia, Canada (Fig. 1), in an area where the Triassic Montney Formation is undergoing extensive development as a major unconventional resource play (Rivard et al., 2014, Gibson and Barclay, 1989). Within the area of interest (AOI) for this study, the Montney Formation consists of fine grained, low-permeability siltstones with porosity < 8% and a vertical thickness > 200 m. The Montney Formation overlies massive carbonates of the Debolt Formation, which in turn overlies a thick shale sequence, the Banff Formation. The northern part of the Montney play, west and north of the AOI, is known to be prone to induced seismicity during HF (Schultz et al., 2020) (Fig. 1).

The Rocky Mountains, located west of the AOI, provide a classic example of a foreland thrust-and-fold belt. This contractional orogen is characterized by thin-skinned tectonics, with no significant involvement of Precambrian crystalline basement (Lebel et al., 1996). In the late stages of this orogen, tectonic shortening within the AOI, located in the foreland of the thrust belt, occurred through fault-propagation folds underlain by foreland- and hinterland-dipping blind thrust (Yeats and Lillie, 1991). In general, these faults flatten out and sole into the Banff Formation, which forms a basal décollement zone throughout the region (Chapman and DeCelles, 2015). At a deeper level, the underlying Precambrian basement is transected by a number of older faults and shear zones (Ross et al., 1994) that mainly strike in a SW-NE direction (Fig. 1).

Induced seismicity that is investigated in this study occurred over a period of two weeks during hydraulic-fracturing operations in two horizontal wells. The events fall within the microearthquake range (Eaton, 2018), with a maximum moment magnitude (M_W) of 1.78, calculated based on seismic moment determined from the low-frequency plateau of the displacement spectrum (Stork et al., 2014). Using Aki's maximum-likelihood method (Aki, 1965), the recorded seismicity is characterized by Gutenberg-Richter *b*-value (slope of the semilogarithmic magnitude-frequency distribution) of ~ 1.16 (Fig. 1), where the minimum magnitude of completeness was obtained using the peak of the non-cumulative magnitude distribution (Wiemer and Wyss, 2000). This parameter provides information about the relative distribution of earthquake magnitudes and may be an indicator of scaling behavior of fracture systems and changes in stress (Igonin et al., 2018, Maxwell et al., 2009). The orientation of maximum horizontal stress is about N55° (i.e., approximately perpendicular to two horizontal wells).

3. Methods

The passive seismic waveform data used in this study were recorded using a dense seismograph array with 27 stations (see Supplementary Fig. 1). The seismometers were buried to the depth of 1 m and comprised of a mix of five broadband seismometers and twenty-two 4.5 Hz three-component geophones (Riazi et al., 2020).

3.1. LinEpiLoc method

LinEpiLoc is a Linear Epicenter Location method which is based on the normal moveout (NMO) equation (Rodríguez-Pradilla, 2019)

$$t^2 = t_0^2 + \frac{x^2}{v^2} \quad , \tag{1}$$

where x is offset or distance, t is travel-time of P- or S-waves, and v is the RMS velocity (P-wave or S-wave) between elevation of receivers and the depth of the induced event. This equation reduces to a linear relationship when t^2 is plotted against x^2. The resulting straight-line slope is v^2 and makes the computation very fast and simple to execute (Rodríguez-Pradilla, 2019). An advantage of this method is the lack of velocity model requirement in the location detection calculations. The epicenter is determined by maximizing R^2 (goodness of fit to a straight line) for all possible locations using a grid-search approach. The location with the highest R^2 value is selected as the epicenter. Supplementary Fig. 5 shows the t^2 and x^2 plot with an induced event from the case study.

3.2. Focal-time method

The velocity-model independent method for determining hypocenters uses two steps: first, the epicenter is estimated based on the minimum travel time location at the surface, by interpolating arrival-time picks (Rodriguez-Pradilla and Eaton, 2020); next, the event depth is determined using a modified form of the focal-time method (Riazi et al., 2020). The focal-time method relies on an implicit time-depth relationship that is established by correlating reflections between conventional P-wave 3-D seismic data and 3-D P-Sv seismic data. In this case, the 3-D seismic data were recorded using 3-component geophones. Since waves radiated by the induced seismic events and waves recorded during the 3-D seismic survey pass through the same medium, this horizon-correlation procedure provides a robust and independent approach to map the zero-offset S-P time from the microseismic events into depth.

The focal-time method requires the phase arrival time, 3-D multicomponent surface seismic data, and station parameters (Riazi et al., 2020, Poulin et al., 2019). A distinct advantage of this method compared to other well-known location detection methods such as NonLinLoc (Lomax, 2005), HypoDD method (Waldhauser and Ellsworth, 2000) and GrowClust (Trugman and Shearer, 2017) is that the focal-time method does not require an explicit velocity model for hypocenter depth location. The basic concept of the focal-time analyses is that time difference between PS time (t_{PS}) and PP time (t_{PP}) from seismic analyses in Eq. 2 is equivalent to the intercept of P- and S-wave phase picks in $t^2 - x^2$ space

$$T_S - T_P|_{x=0} \cong t_{PS} - t_{PP} \tag{2}$$

where T_S and T_P are S-wave and P-wave time from induced/microseismic data and x represents the offset. The statics corrections are needed to ensure that both passive seismic observations and 3-D seismic data share a common datum in areas of moderate to high topography (Riazi et al., 2020, Poulin et al., 2019).

3.3. Fault Slip Potential

We used the fault slip potential method, freely available at the Stanford Center for Induced and Triggered Seismicity (Walsh III et al., 2018), as a probabilistic screening tool for faults and structural zones near treatment wells in the AOI. The program is based on the quantitative risk assessment applied to geomechanics with following input parameters: fault strike and dip, well locations, and mechanical stress state parameters (Walsh III et al., 2018). The program first calculates the Mohr-Coulomb pore pressure to slip on each fault using deterministic technique and then it performs Monte-Carlo analysis based on prior distributions of input parameters to determine the probability of fault slipping as a function of pore-pressure change.

3.4. Structural Interpretation

Seismic structural interpretation is performed based on the 3-D depth-migrated seismic data with the aid of seismic attributes in the AOI. The seismic horizons and faults were interpreted in every line and crossline of the seismic data, through manual picking. We also checked the 3-D view of faults and seismic horizons to manage consistent interpretation of horizons and faults. For the faults orientated in different direction of the vertical seismic section, we used seismic attributes, which effectively help us detect the fault morphology on different depth slices. Structural features such as faults and folds often change the dip and azimuth of the seismic reflection and the use of seismic attributes aids in their efficient interpretation.

4. Results

4.1. Structural seismic interpretation.

Fig. 2 shows horizontal and vertical slices extracted from the 3-D seismic data. The studied seismic survey is a 3-D depth-migrated dataset with high signal-to-noise ratio within the bandwidth from 8-120 Hz. Thrust ramps are clearly evident based on structural offsets of layer boundaries and partially imaged fault planes. These thrust ramps are separated from each other by approximately 2 km; they terminate upwards into anticlines and sole downwards into the Banff Formation, a thick shale sequence that forms a regional décollement (Chapman and DeCelles, 2015). Depth slices in the left panel illustrate variance maps for different three depth locations below the injection level (Montney). The variance attribute calculates local variance in the seismic signal based on the statistical properties of immediately neighbouring data samples in the 3-D cube. This seismic attribute accentuates reflection discontinuities; in this case, the primary structural grain, trending N15°W, is defined by the intersection of gently dipping reflections with the horizontal surface of the depth slice. This structural grain is sub-parallel to the strike of the thrust ramps as well as the Rocky Mountain deformation front west of the AOI. Fig. 3 shows an example of a thrust fault (F4), located at the west of horizontal wells. The orientation of thrust faults presented in this paper (F1 to F4) is-parallel to the strike of the thrust ramps in the region, as well as the Rocky Mountain deformation front west of the AOI.

Quasi-linear transverse structures are also apparent in each depth slice, especially in the upper stratigraphic levels of the Debolt Formation. These transverse structures exhibit a slight rotation in orientation with increasing depth. By analogy with the structural style mapped in the Rockies (McMechan, 2012), these features are likely fold hinges and/or tear faults that transfer displacement between thrust ramps. Transverse structures are mainly subparallel to the shear zones in the region as shown in Fig. 1. The location and orientation of these transverse structures may be inherited from Precambrian basement faults (McMechan, 2012). In a nearby study in the Fort St. John area, Roth et al. (2020) determined the orientation of strike-slip faults, perpendicular to thrust faults, by relative relocations and the progressive migration of seismicity. The use of 3-D seismic data to image these structures, as in our study, has the potential advantage that these structures can be identified in advance of hydraulic-fracturing operations.

4.2. Induced seismicity

Fig. 2 shows the hypocenter locations of events whose epicenters are located within 200m of the plane of the profile. The projection of these hypocenters into this plane shows that the thrust ramps of faults F2 and F3 were likely activated during HF operations at the two wells. Importantly, the induced seismicity occurred below the depth level of the wells where hydraulic fracturing occurred in the Montney Formation. Indeed, virtually all of the induced events occur within massive carbonates of the Mississippian Debolt Formation, a thick, mechanically strong layer that effectively makes the Debolt Formation more susceptible to hosting larger seismic events.

Fig. 4 shows the location of all of the induced seismic events in relation to the two horizontal wells. The symbols are colored according to the time of occurrence and scaled (in size) based on event magnitude. Most of the events occurred below the two wells, likely on, or near, fault F3. However, the largest event, M_W 1.78, occurred nearly 2 km east of the wells on fault F4, three days after the start of the HF program. A profile extracted from the 3-D cube showing the seismic expression of fault F4 is presented in Fig. 3. A set of smaller events west and north of wells A and B occurred along fault F2, delineating the fault plane (in map view). These events occurred near the end of the program and migrated progressively along this linear zone in a NNW direction. Finally, a set of weak events close to the injection zone extends a short distance away from the wells (arrows in Fig. 4), apparently along a transverse structure in the upper Debolt Formation that was identified in the 3-D seismic data (Fig. 2). The largest event on fault F4 appears to correspond with the point of intersection of the transverse structure with the fault. This event produced small aftershocks along this trend. In addition, the activated segment of fault F2 appears to be bounded, at its southern limit, by the intersection of this fault with the same transverse structure. This event sequence initiated near the apparent intersection of the transverse structure with the fault and then migrated away from this intersection point.

5. Discussion

5.1. Fault activation mechanism

A number of distinct fault-triggering mechanisms have been proposed to explain induced earthquakes associated with HF (Eaton, 2018, Atkinson et al., 2020, Schultz et al., 2020, Kettlety et al., 2020). These mechanisms include: reduction in effective normal stress due to pore-pressure increase resulting from intersection of a fault zone by a hydraulic fracture (Maxwell et al., 2009, Bao and Eaton, 2016); pore-pressure increase due to diffusion into a fault from the HF-stimulated region close to the injection wells (Atkinson et al., 2016); elastostatic stress transfer due to the tensile opening of hydraulic fractures (Kettlety et al., 2020); poroelastic stress coupling between hydraulic fractures and fault zones (Deng et al., 2016); and fault loading due to aseismic fault creep (Eyre et al., 2019a). Important clues to distinguish between these different activation mechanisms can be discerned from the spatiotemporal pattern of induced events with respect to the HF program.

The most direct activation mechanism is intersection of a pre-existing fault by a hydraulic fracture (Bao and Eaton, 2016, Maxwell et al., 2009). In this case, injection of highly pressurized fluids increases the pore-fluid pressure within the fault and thus reduce the effective stress, leading to frictional failure. However, the distance from the HF wells to the activated faults (F2 and F4), as well as the orientation of zones of seismicity, are inconsistent with this mechanism. Hydraulic fractures are expected to occur within the treatment zone (Montney Formation) with orientations parallel to the maximum horizontal stress (SHmax) direction (i.e. approximately perpendicular to wells A and B). Events with this expected geometry are not clearly expressed in our data, most likely because the magnitude of these events (generally M < 0 (Eaton, 2018)) is less than the detection threshold of the monitoring network. Nevertheless, the half-length of hydraulic fractures is expected to be no more than several hundred meters (Yu et al., 2014), which is considerably less than the observed activation distance of up to 2 km. Consequently, it is very unlikely that faults F2 and F4 were directly pressurized by intersection with a hydraulic fracture.

An alternative mechanism involves pressure diffusion through a porous medium from the stimulated (pressurized) part of the reservoir located near the HF wells (Shapiro and Dinske, 2009). However, for triggering distance of up to 2 km as observed in this study, matrix diffusion through the low-permeability Montney Formation (in practice, virtually any tight formation that requires HF in order to produce hydrocarbons) would require a much longer time span than the observed timescale of days (e.g., Atkinson et al., 2016). The possibility of a high-permeability pathway for diffusion is discussed below.

Poroelastic stress coupling is expected to occur on a sufficiently short timescale and could reach as far as 2km (Deng et al., 2016). While this mechanism could thus explain the observed activation of fault F4, it cannot explain a number of other observed characteristics in our data, including: apparent progressive migration of weak seismicity along fault F2; localization of patterns of seismicity near the points of intersection of transverse structures and fault ramps; and evidence for linear trends of weak seismicity along transverse structures.

Eyre et al. (2019a) proposed a model for fault triggering during HF by aseismic creep. This model invokes rate-strain frictional behavior and is generally applicable to a critically stressed fault that cuts through an injection zone that is clay- and organic-rich formation – typical for many shales that are targeted by HF. Rocks with this composition are likely to be subject to velocity strengthening (Kohli and Zoback, 2013). According to this model, fault pressurization during HF leads to aseismic creep in the velocity-strengthening part of the fault, which progressively loads other parts of the fault and ultimately could lead to rupture nucleation on an unstable fault patch.

This mechanism could explain the observed activation of thrust ramp F3 in the Debolt Formation below the HF zone, particularly in view of the lithological similarities between the Debolt Formation and thick carbonates in the area studied by Eyre et al. (Eyre et al., 2019b), but since the transverse structures do not appear to extend upwards into the Montney Formation, it does not entirely explain the activation of faults F2 and F4.

Finally, we consider a hypothesis that the thrust ramps (F2, F3 and F4) are connected by transverse structures that serve as pathways for relatively rapid pore-pressure diffusion throughout the fault network. If so, the permeability of these zones would need to be sufficient to enable fault activation on a timescale of days and a distance of up to 2 km. Based on a semi-analytical model to explain the observed spatio-temporal seismicity characteristics, we estimate that the required hydraulic diffusivity, a measure of the speed at which a finite pressure pulse will propagate through a permeable system, is > 4 m^2/s (Supplementary Fig. 4), at least two orders-of-magnitude greater than expected for unfractured matrix of the Montney Formation (Riazi et al., 2020). Similar scenarios of pore-pressure diffusion along highly permeable pathways (fracture zones) in the Duvernay play in Alberta, Canada provide an explanation for fault activation at distances of up to 2 km and time lags of 2-4 days (Galloway et al., 2018, Igonin et al., 2020, Schultz & Wang, 2020). A comparable model has been developed for the Montney Formation by Peña Castro et al. (2020), where the mainshock occurred 2 km below the injection zone, in the basement, about 2 days following the onset of injection. Peña Castro et al. (2020) indicate that no physical/seismic evidence of such conduit was known prior to the induced event. Using a numerical simulation approach and assuming a minimum pressure increase of 0.2 MPa for fault activation, they fit their observations using a 2-10m thick permeable zone with permeability of 150 – 230 mD (1 D ~ 1 μm^2).

Since seismicity observed along the transverse structures is weak, one of the implications of this model is that pore-pressure diffusion along these pathways occurs in a nearly aseismic manner.

To evaluate whether this is consistent with available information about the state of stress and fault geometry, the next section applies a probabilistic screening tool to characterize fault activation.

5.2. Fault slip potential (FSP)

Fault Slip Potential is used as a screening tool (Walsh III et al., 2018) to estimate the probability of fault slip and the sensitivity of failure to the input model parameters. In this study, where faults are well imaged by 3-D seismic data and measured pore pressure data are available, some parameters such as fault strike and dip have atypically low uncertainties, but other parameters such as absolute stress magnitude and coefficient of static friction have higher levels of uncertainty.

Fig. 5 shows a 3-D view of the fault system within the Debolt Formation based on seismic data, depicting the results of FSP analysis for thrust ramps (F2, F3 and F4) as well as the interpreted transverse structure. Each fault is colored based on the nominal pore pressure increase required to induce fault slip at a 50% level of likelihood, based on our modelling. Due to their more favourable orientation relative to the regional stress field, this analysis shows that the transverse structure is farther from failure (i.e., a considerably larger pore pressure increase is needed to bring them to failure) than the thrust ramps. This result is consistent with relatively aseismic behavior of pore-pressure diffusion along the transverse faults. Recent studies based on direct measurements of fluid injected into a fault (Guglielmi et al., 2015) and hydromechanical modeling (Cappa et al., 2018) indicate that increases in permeability accompany aseismic slip processes. These results support our interpretation that transverse faults could be aseismic, but nevertheless provide enhanced-permeability conduits for pore-pressure diffusion. If this is correct and transverse structures provide permeable pathways between thrust faults, this provides a cautionary message for relying entirely on microseismicity to track seismicity triggering fronts (Shapiro et al., 2003).

5.3. Fault-system behavior

As part of the evolution of foreland fault systems that developed during tectonic shortening associated with orogenic development of the Canadian Rocky Mountains, transverse faults transferred displacement between individual thrust sheets (Mcmechan and Thompson, 1989). The location and orientation of these transverse faults were likely influenced by the structural fabric of the underlying Precambrian basement and may preserve a connection into the basement (McMechan, 2012). When considered holistically as a fault system, our data suggest that these features continue to exert a significant influence in terms of activation of induced seismicity. Here, they are interpreted to provide permeable pathways that allow pore-pressure (and possibly stress) communication between different thrust ramps. In addition, the intersections of these transverse structures with thrust ramps in the Debolt Formation appears to play a role in localizing the seismicity response (Fig. 4). In intraplate regions such as our AOI, such points of intersection have been interpreted to be loci of anomalous stress concentrations within the contemporary stress field (Talwani, 1988). Taken together, these observations suggest that, in addition to considering mapped faults that are favourably oriented for slip in the present-day stress field, pre-operational risk analysis should consider possible the potential for permeable pathways that could connect faults with the stimulated region as well as stress concentrations at the intersection of different structural elements.

6. Conclusions

The detailed anatomy of a buried thrust fault system is imaged in this study using high-resolution, depth-migrated 3-D seismic data. Induced events that occurred during a 2-week hydraulic-fracturing program in the Montney Formation were located based on data from a local seismograph network, using a novel methodology that does not require an explicit velocity model. Hypocenters of most of the induced events occurred on (or near) thrust ramps within the Debolt Formation, a massive carbonate unit that represents geomechanical basement below the

Montney Formation. Our analysis suggests that transverse structures have retained sufficient permeability to allow pore-pressure diffusion to occur aseismically on a distance scale of up to 2 km and a timescale of 3-14 days. From a fault-system perspective, our results suggest that transverse structures continue to interact with thrust ramps, with respect to transfer of stress and fluid-pressure. In addition, the intersections of transverse structures with thrust faults could form stress concentrations that localize induced seismicity behavior. These factors provide new considerations that are likely to be important in pre-operational seismic risk assessment.

Data Availability

All seismic sections needed to interpret structural features and evaluate the conclusions of the paper are illustrated in the paper. Continuous waveform data for this region is available online at the Incorporated Research Institutions for Seismology (https://ds.iris.edu/mda/EO/). Earthquake catalog of the Natural Resources Canada (NRCan) used in Fig. 1 can be downloaded from https://earthquakescanada.nrcan.gc.ca/stndon/NEDB-BNDS/bulletin-en.php. Well log data and HF completion data can be freely downloaded from the BC Oil and Gas Commission website https://www.bcogc.ca/energy-professionals/online-systems/.

Code availability

The focal-time python codes used in this study are available on request from the corresponding author.

Author Contributions

Naimeh Riazi performed the data analysis and figure preparation. Both authors collaborated in project conceptualization and writing the manuscript.

Competing interests

The authors declare no competing interests.

Acknowledgments

Sponsors of the Microseismic Industry Consortium are sincerely thanked for their support of this initiative. ConocoPhillips Company, Pulse Seismic, and TGS Canada Corp. are thanked for providing the seismic dataset for this study. We are also grateful for discussions with Alemayehu Aklilu, Thomas Eyre and German Rodriguez Pradilla. This work was supported in part by the Canada First Research Excellence fund and by NSERC grant CRDPJ/474748-2014.

References

Abe S, Suzuki N. Complex-network description of seismicity. Vol. 13. 2006.

Aki K. Maximum likelihood estimate of b in the formula log N = a-bM and its confidence limits. Bull Earthq Res Inst, Tokyo Univ 1965;43:237–9.

Alt RC, Zoback MD. In situ stress and active faulting in Oklahoma. Bull Seismol Soc Am 2017;107:216–28. https://doi.org/10.1785/0120160156.

Atkinson GM, Eaton DW, Ghofrani H, Walker D, Cheadle B, Schultz R, et al. Hydraulic Fracturing and Seismicity in the Western Canada Sedimentary Basin. Seismol Res Lett 2016;87:631–47. https://doi.org/10.1785/0220150263.

Atkinson GM, Eaton DW, Igonin N. Developments in understanding seismicity triggered by hydraulic fracturing. Nat Rev Earth Environ 2020;1:264–77. https://doi.org/10.1038/s43017-020-0049-7.

Attanayake J, Sandiford D, Schleicher LS, Jones A, Gibson G, Sandiford M. Interacting Intraplate Fault Systems in Australia: The 2012 Thorpdale, Victoria, Seismic Sequences. J Geophys Res Solid Earth 2019;124:4673–93. https://doi.org/10.1029/2018JB016945.

Bao X, Eaton DW. Fault activation by hydraulic fracturing in western Canada. Science (80-)

2016;354:1406–9. https://doi.org/10.1126/SCIENCE.AAG2583.

Burwash RA, McGregor CR, Wilson J. Chapter 5 - Precambrian Basement Beneath the Western Canada Sedimentary Basin. Geol Atlas West Canada Sediment Basin, Can Soc Pet Geol Alberta Res Counc 1994:49–57.

Cappa, F., Guglielmi, Y., Nussbaum, C., Birkholzer, J. On the relationship between fault permeability increases, induced stress perturbation, and the growth of aseismic slip during fluid injection. Geophysical Research Letters, 2018; 45(20), 11-012.

Chapman JB, DeCelles PG. Foreland basin stratigraphic control on thrust belt evolution. Geology 2015;43:579–82. https://doi.org/10.1130/G36597.1.

Deng K, Liu Y, Harrington RM. Poroelastic stress triggering of the December 2013 Crooked Lake, Alberta, induced seismicity sequence. Geophys Res Lett 2016; 43:8482–91. https://doi.org/10.1002/2016GL070421.

Eaton DW. Passive seismic monitoring of induced seismicity: Fundamental principles and application to energy technologies. Cambridge University Press, 2018.

Eaton, DW, Igonin, N, Poulin, A, Weir, R, Zhang, H, Pellegrino, S, Rodriguez, G. Induced seismicity characterization during hydraulic-fracture monitoring with a shallow-wellbore geophone array and broadband sensors. Seismological Research Letters, 2018; 89(5), 1641-1651.

Ellsworth WL. Injection-Induced Earthquakes. Science (80-) 2013;341:1225942–1225942. https://doi.org/10.1126/science.1225942.

Eyre TS, Eaton DW, Garagash DI, Zecevic M, Venieri M, Weir R, et al. The role of aseismic slip in hydraulic fracturing–induced seismicity. Sci Adv 2019a;5:eaav7172. https://doi.org/10.1126/sciadv.aav7172.

Eyre TS, Eaton DW, Zecevic M, D'amico D, Kolos D. Microseismicity reveals fault activation before M w 4.1 hydraulic-fracturing induced earthquake. Geophys J Int 2019b;218:534–46. https://doi.org/10.1093/gji/ggz168.

Gibson DW, Barclay JE. Middle Absaroka Sequence The Triassic Stable Craton. Can Soc Pet Geol Spec Publ No 30 1989:219–32.

Gray DR, Janssen C, Vapnik Y. Deformation character and palaeo-fluid flow across a wrench fault within a Palaeozoic subduction-accretion system: Waratah fault zone, southeastern Australia. J Struct Geol 1999;21:191–214. https://doi.org/10.1016/S0191-8141(98)00115-1.

Guglielmi, Y., Cappa, F., Avouac, J. P., Henry, P., Elsworth, D. Seismicity triggered by fluid injection–induced aseismic slip. Science, 2015; 348(6240), 1224-1226.

Hennings PH, Snee JEL, Osmond JL, Deshon HR, Dommisse R, Horne E, et al. Injection-induced seismicity and fault-slip potential in the fort worth basin, Texas. Bull Seismol Soc Am 2019;109:1615–34. https://doi.org/10.1785/0120190017.

Igonin N, Verdon JP, Kendall JM, Eaton DW. Large-scale fracture systems are permeable pathways for fault activation during hydraulic fracturing. J Geophys Res - Solid Earth Submitt 2020.

Igonin N, Zecevic M, Eaton DW. Bilinear Magnitude-Frequency Distributions and Characteristic Earthquakes During Hydraulic Fracturing. Geophys Res Lett 2018;45:12,866-12,874. https://doi.org/10.1029/2018GL079746.

Jones GA, Kendall JM, Bastow ID, Raymer DG. Locating microseismic events using borehole data. Geophys Prospect 2014;62:34–49. https://doi.org/10.1111/1365-2478.12076.

Kettlety T, Verdon JP, Werner MJ, Kendall JM, Budge J. Investigating the role of elastostatic stress transfer during hydraulic fracturing-induced fault activation. Geophys J Int 2019;217:1200–16. https://doi.org/10.1093/gji/ggz080.

Kohli AH, Zoback MD. Frictional properties of shale reservoir rocks. J Geophys Res Solid Earth 2013;118:5109–25. https://doi.org/10.1002/jgrb.50346.

Langenbruch C, Zoback MD. Response to Comment on “How will induced seismicity in Oklahoma respond to decreased saltwater injection rates?” vol. 3. 2017. https://doi.org/10.1126/sciadv.aao2277.

Lebel D, Langenberg W, Mountjoy EW. Structure of the central Canadian Cordilleran thrust-and-fold belt, Athabasca-Brazeau area, Alberta: a large, complex intercutaneous wedge 1. vol. 44. 1996.

Lomax A. A Reanalysis of the Hypocentral Location and Related Observations for the Great 1906 California Earthquake. Bull Seismol Soc Am 2005;95:861–77. https://doi.org/10.1785/0120040141.

Mahani AB, Kao H, Atkinson GM, Assatourians K, Addo K, Liu Y. Ground-motion characteristics of the 30 November 2018 injection-induced earthquake sequence in northeast British Columbia, Canada. Seismol Res Lett 2019;90:1457–67. https://doi.org/10.1785/0220190040.

Maxwell SC, Jones M, Parker R, Miong S, Leaney S, Dorval D, et al. Fault activation during hydraulic fracturing. 2009. https://doi.org/10.3997/2214-4609.201400770.

McMechan ME. Deep transverse basement structural control of mineral systems in the southeastern Canadian Cordillera. Can J Earth Sci 2012;49:693–708. https://doi.org/10.1139/E2012-013.

McMechan ME, Thompson RI. Structural Style and History of the Rocky Mountain Fold and Thrust Belt. 1989.

Peña-Castro, A.F., Roth, M.P., Verdecchia, A., Onwuemeka, J., Liu, Y., Harrington, R.M., Zhang, Y. and Kao, H., Stress chatter via fluid flow and fault slip in a hydraulic fracturing induced earthquake sequence in the Montney formation, British Columbia. Geophysical Research

Letters, 2020. e2020GL087254.

Pondard N, Armijo R, King GCP, Meyer B, Flerit F. Fault interactions in the Sea of Marmara pull-apart (North Anatolian Fault): earthquake clustering and propagating earthquake sequences. Geophys J Int 2007;171:1185–97. https://doi.org/10.1111/j.1365-246X.2007.03580.x.

Poulin A, Weir R, Eaton D, Igonin N, Chen Y, Lines L, et al. Focal-time analysis: A new method for stratigraphic depth control of microseismicity and induced seismic events. Geophysics 2019;84:1–45. https://doi.org/10.1190/geo2019-0046.1.

Price RA. Cordilleran Tectonics and the Evolution of the Western Canada Sedimentary Basin 1994.

Riazi N, Eaton DW, Aklilu A, Poulin A. Application of Focal-Time Analysis for Improved Induced Seismicity Depth Control: A Case Study from the Montney Formation, British Columbia, Canada. Geophysics, 2020; 85(6), 1-70.

Rivard C, Lavoie D, Lefebvre R, Séjourné S, Lamontagne C, Duchesne M. An overview of Canadian shale gas production and environmental concerns. Int J Coal Geol 2014;126:64–76. https://doi.org/10.1016/j.coal.2013.12.004.

Rodríguez-Pradilla G. Microseismic Monitoring of a Duvernay Hydraulic-Fracturing Stimulation, Alberta Canada: Processing and Interpretation assisted by Finite-Difference Synthetic Seismograms. Univeristy Calgary, PhD Thesis 2019.

Rodríguez-Pradilla, G., Eaton, D. W. Automated Microseismic Processing and Integrated Interpretation of Induced Seismicity during a Multistage Hydraulic-Fracturing Stimulation, Alberta, Canada. Bulletin of the Seismological Society of America, 2020; 110(5), 2018-2030.

Ross GM, Broome J, Miles W. Potential Fields and Basement Structure - Western Canada Sedimentary Basin. Geol Atlas West Canada Sediment Basin, Can Soc Pet Geol Alberta Res Counc 1994:41.

Roth MP, Verdecchia A, Harrington RM, Liu Y. High-Resolution Imaging of Hydraulic-Fracturing-Induced Earthquake Clusters in the Dawson-Septimus Area, Northeast British Columbia, Canada. Seismological Research Letters. 2020 Sep;91(5):2744-56.

Rundle PB, Rundle JB, Tiampo KF, Martins JSS, Mcginnis S, Klein W. Nonlinear Network Dynamics on Earthquake Fault Systems 2001. https://doi.org/10.1103/PhysRevLett.87.148501.

Schultz R, Skoumal RJ, Brudzinski MR, Eaton DW, Baptie B, Ellsworth WL. Hydraulic Fracturing Induced Seismicity. Rev Geophys Press 2020.

Shapiro SA, Dinske C. Fluid-induced seismicity: Pressure diffusion and hydraulic fracturing. Geophys. Prospect., vol. 57, Blackwell Publishing Ltd; 2009, p. 301–10. https://doi.org/10.1111/j.1365-2478.2008.00770.x.

Shapiro SA, Patzig R, Rothert E, Rindschwentner J. Triggering of Seismicity by Pore-pressure Perturbations: Permeability-related Signatures of the Phenomenon. Thermo-Hydro-Mechanical Coupling Fract. Rock, Birkhäuser Basel; 2003, p. 1051–66. https://doi.org/10.1007/978-3-0348-8083-1_16.

Speight JG. Handbook of Hydraulic Fracturing. Hoboken, NJ: wiley; 2016. https://doi.org/10.1002/9781119225102.

Spotila JA, Anderson KB. Fault interaction at the junction of the Transverse Ranges and Eastern California shear zone: A case study of intersecting faults. Tectonophysics 2004;379:43–60. https://doi.org/10.1016/j.tecto.2003.09.016.

Stork, A. L., Verdon, J. P., Kendall, J. M. The robustness of seismic moment and magnitudes estimated using spectral analysis. Geophysical Prospecting, 2014; 62:862-878.

Talwani P. The intersection model for intraplate earthquakes. Seismol Res Lett 1988;59:305–10. https://doi.org/10.1785/gssrl.59.4.305.

Trugman DT, Shearer PM. GrowClust: A Hierarchical Clustering Algorithm for Relative Earthquake Relocation, with Application to the Spanish Springs and Sheldon, Nevada, Earthquake Sequences. Seismol Res Lett 2017;88:379–91. https://doi.org/10.1785/0220160188.

Waldhauser F, Ellsworth WL. A Double-Difference Earthquake Location Algorithm: Method and Application to the Northern Hayward Fault, California. vol. 90. 2000.

Walsh III R, Zoback MD, Lele SP, Pais D, Weingarten M, Tyrrell T. FSP 2.0: A PROGRAM FOR PROBABILISTIC ESTIMATION OF FAULT SLIP POTENTIAL RESULTING FROM FLUWalsh III, Rall; Zoback, Mark D.; Lele, Suvrat P.; Pais, Darren; Weingarten, Matthew; Tyrrell, Timothy ;ID INJECTION. Stanford Cent Induc Triggered Seism 2018:1–51.

Wiemer, S., & Wyss, M. Minimum magnitude of completeness in earthquake catalogs: Examples from Alaska, the western United States, and Japan. Bulletin of the Seismological Society of America, 2000; 90(4), 859-869.

Yeats RS, Lillie RJ. Contemporary tectonics of the Himalayan frontal fault system. Folds, blind thrusts and the 1905 Kangra earthquake. J Struct Geol 1991;13:227–33. https://doi.org/10.1016/0191-8141(91)90069-U.

Yu W, Luo Z, Javadpour F, Varavei A, Sepehrnoori K. Sensitivity analysis of hydraulic fracture geometry in shale gas reservoirs. J Pet Sci Eng 2014;113:1–7. https://doi.org/10.1016/j.petrol.2013.12.005.

Zhang H, Thurber CH. Double-Difference Tomography: The Method and Its Application to the Hayward Fault, California. vol. 93. 2003.

Figures

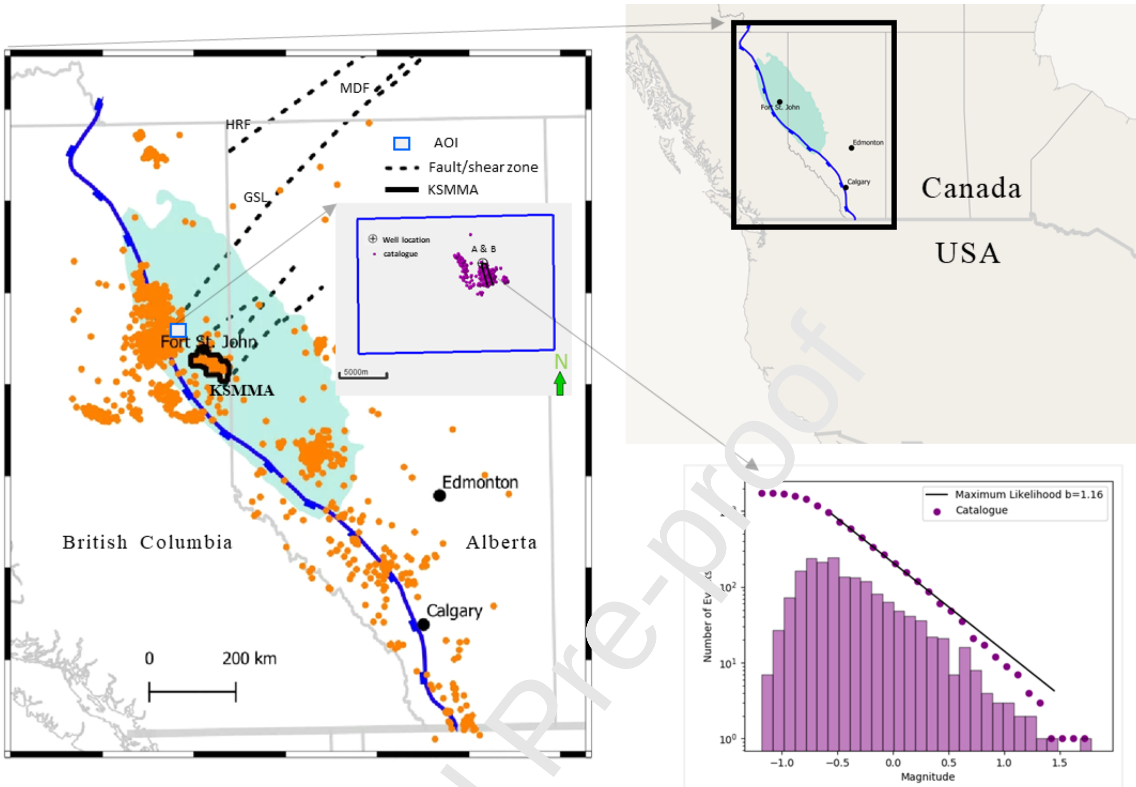

Fig. 1. The Montney unconventional resource play (green area) showing $M_W \geq 2$ seismicity from 2006 to 2020 (orange dots), from Mahani et al. (2019), as well as the location of area of interest (AOI). Blue line with tick marks shows the eastern limit of Cordilleran deformation at the surface, from Price (1994). KSMMA outlines the Kiskatinaw Seismic Monitoring and Mitigation Area, where a recent M4.5 earthquake occurred (Peña-Castro et al., 2020). Faults or shear zone in the Precambrian basement are indicated by dashed black lines (Burwash et al., 1994). GSL, MDF, and HRF denote Great Slave Lake shear zone, McDonald Fault, Hay River fault, respectively. Lower right panel shows magnitude-frequency distribution (non-cumulative and cumulative) based on induced seismicity recorded using a dense seismograph array in the AOI (purple dots). The estimated *b*-value of 1.16, based on an inferred magnitude of completeness of –0.5 M_W, is indicative of likely fault activation during hydraulic-fracturing operations.

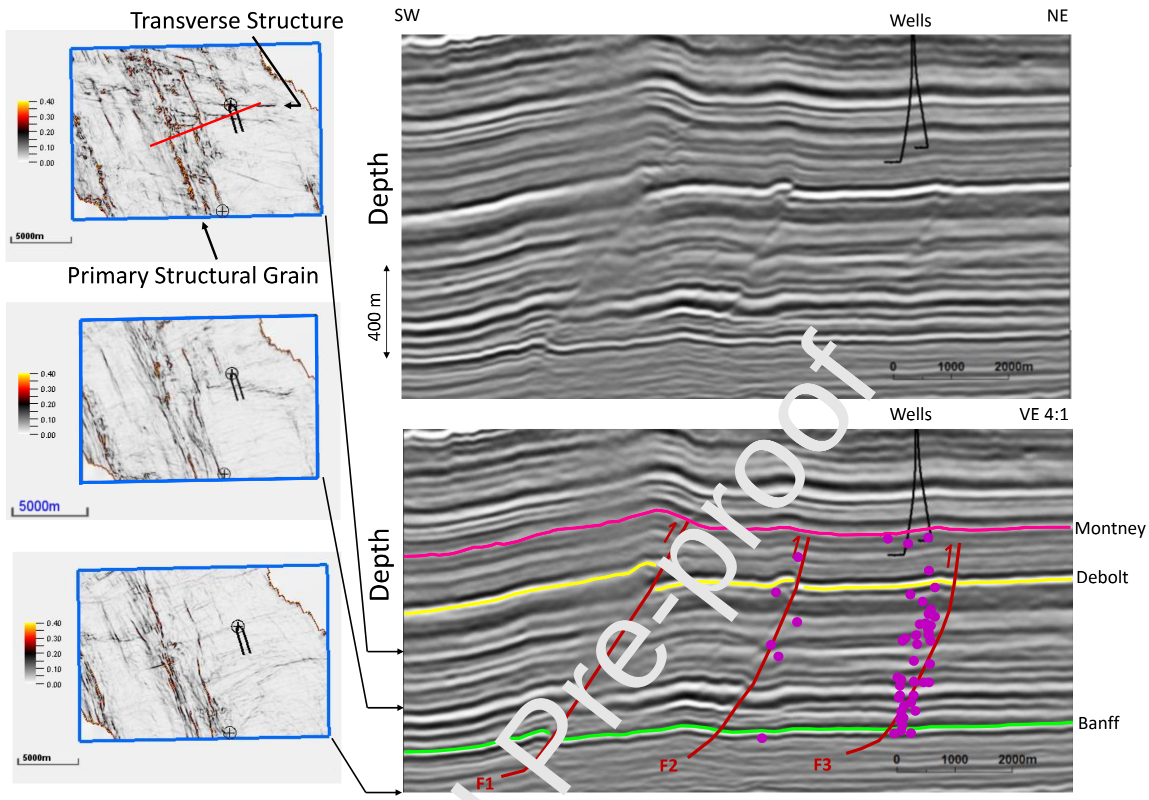

Fig. 2. Images extracted from 3-D seismic data cube. Right panels show uninterpreted (top) and interpreted (lower) ~11-km seismic profile (location shown in top-left panel). F1, F2, F3 are thrust ramps that terminate upwards into anticlines. Magenta dots show hypocenters of induced seismic events projected into the plane of the profile. These events occur mainly within massive carbonates of the Debolt Formation and correlate approximately with faults F2 and F3. Left panels show depth slices (depths are indicated by the arrows at the edge of the profile) depicting variance, a seismic attribute that accentuates reflection discontinuities based on local statistical variance calculated using the seismic data. The location of the profile on the right is shown by a red line and the two wells are shown as black lines. The N15^{o}W primary structural grain is parallel to the strike of the reverse faults. Transverse structures appear as quasi-linear features in the depth sections (left panels) and strike at a high angle to the primary structural grain.

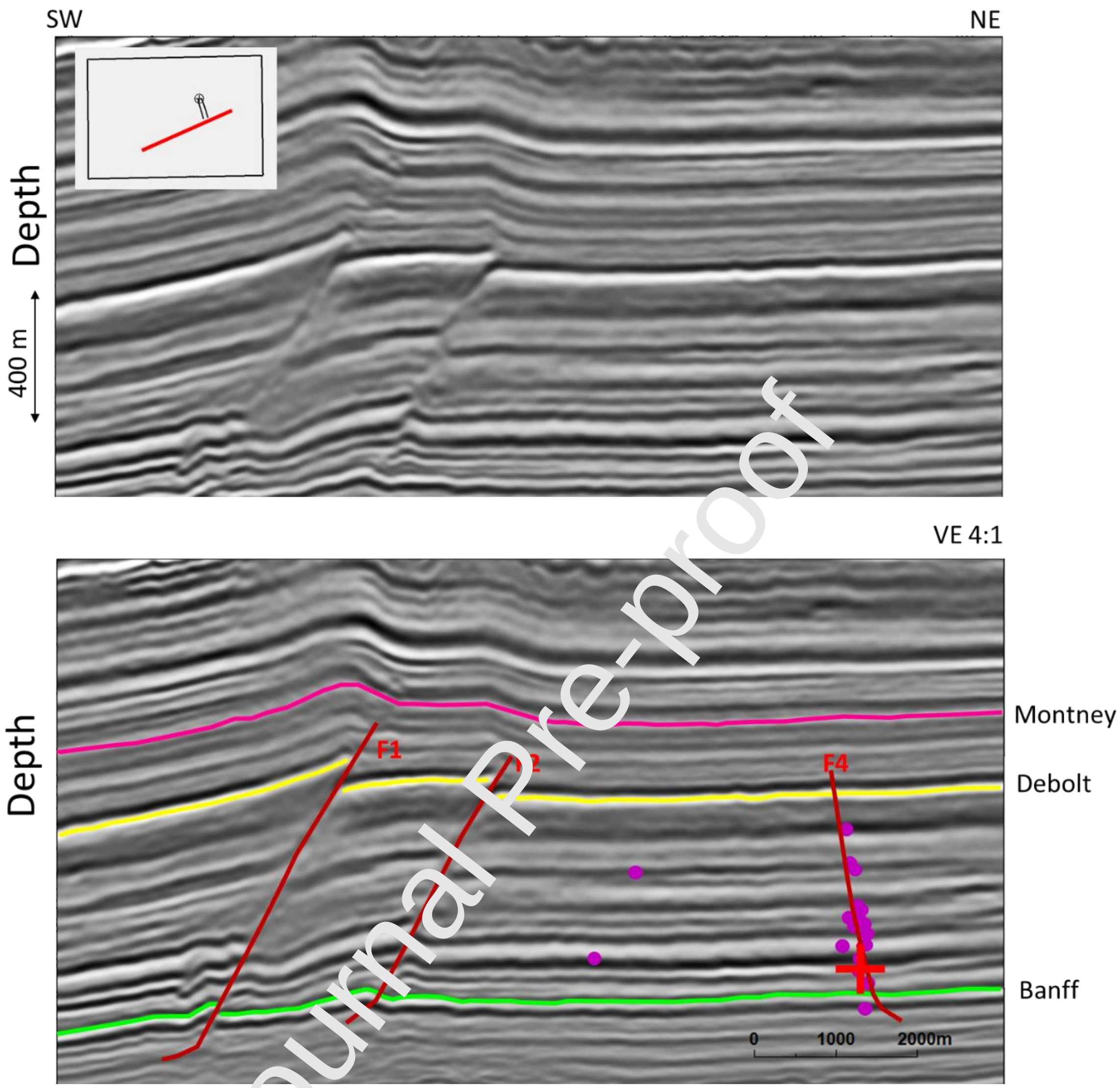

Fig. 3. Seismic imaging of a back-thrust (F4), aided by induced events that occurred about 1.5 km east of the horizontal wells. F1 and F2 are thrust faults that were interpreted using conventional seismic interpretation. Red + symbol shows the location of mainshock (Mw=1.78). The inset shows the location of the seismic section in the AOI.

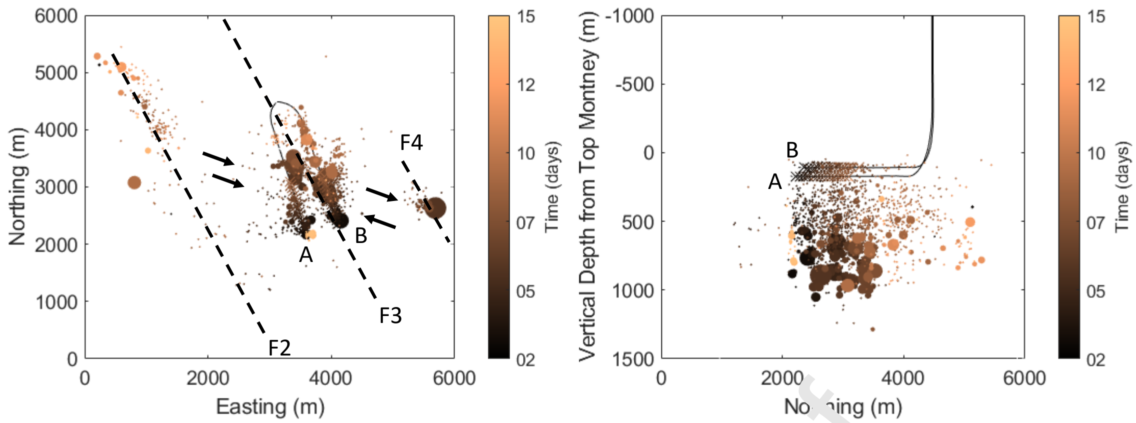

Fig. 4. Location of induced events in map-view (left) and cross section (right) during hydraulic fracturing of Wells A and B. Events are colored by time of occurrence and sized according to magnitude. Stage locations along wells A and B are shown with × symbols. Locations of thrust ramps in the upper Debolt are shown by dashed lines. Arrows indicate interpreted alignment of microseismicity with a transverse structure (Fig. 2) that connects faults F2-F3-F4.

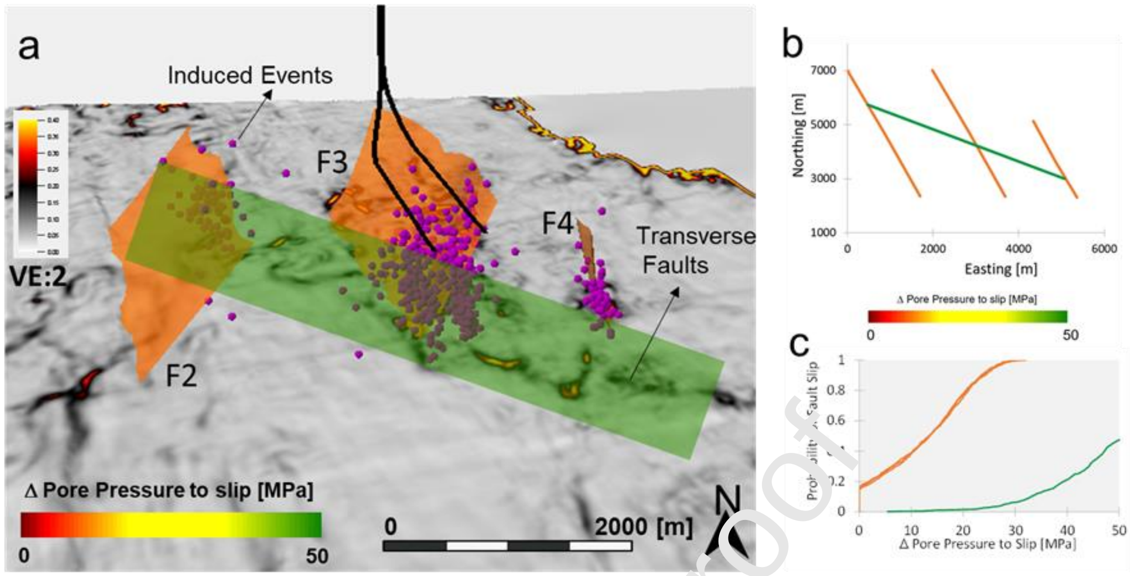

Fig. 5. Summary of fault-slip potential analysis showing 3-D view of interpreted faults adjacent to wells A and B. The variance depth map is also intersected with the fault interpretation with shows the three thrust faults and transverse fault. Faults are colored according to the increase in pore pressure required to bring the fault to failure based on the Mohr-Coulomb criterion with friction μ = 0.6. b shows the plane-view of faults and c is the cumulative distribution function (CDF) of the pore pressure to slip curve for each fault.

Figures

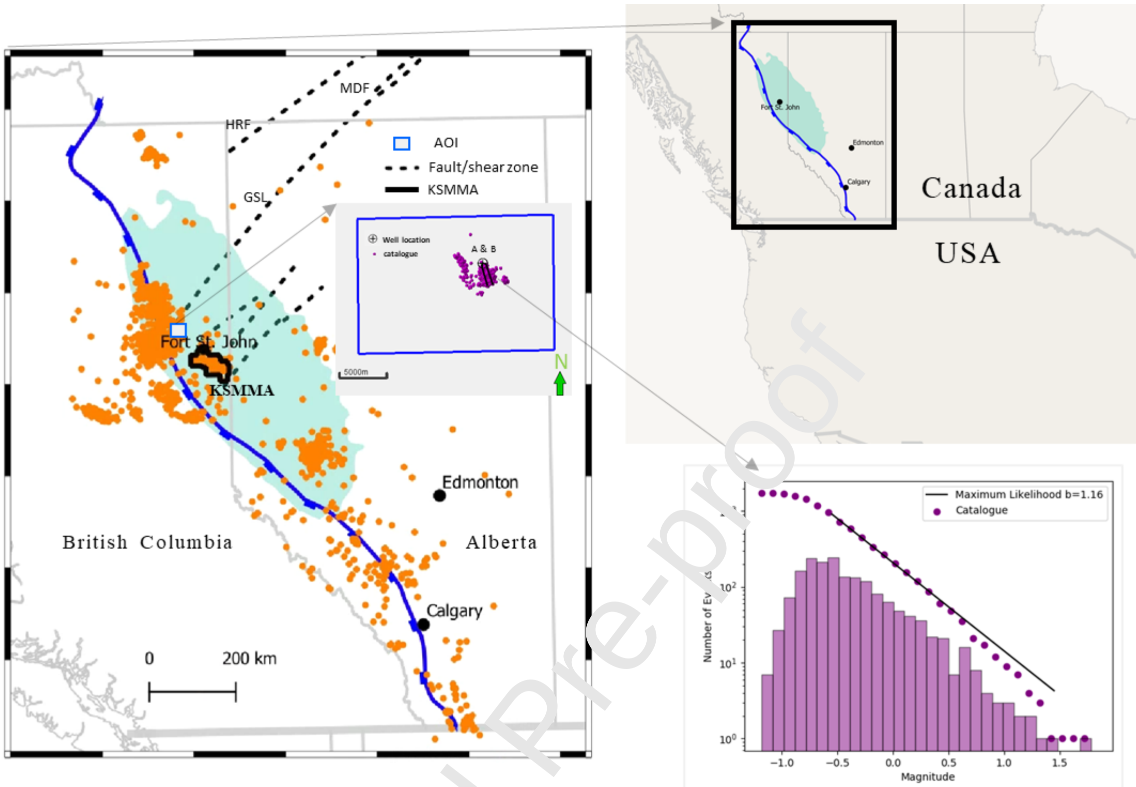

Fig. 1. The Montney unconventional resource play (green area) showing $M_W \geq 2$ seismicity from 2006 to 2020 (orange dots), from Mahani et al. (2019), as well as the location of area of interest (AOI). Blue line with tick marks shows the eastern limit of Cordilleran deformation at the surface, from Price (1994). KSMMA outlines the Kiskatinaw Seismic Monitoring and Mitigation Area, where a recent M4.5 earthquake occurred (Peña-Castro et al., 2020). Faults or shear zone in the Precambrian basement are indicated by dashed black lines (Burwash et al., 1994). GSL, MDF, and HRF denote Great Slave Lake shear zone, McDonald Fault, Hay River fault, respectively. Lower right panel shows magnitude-frequency distribution (non-cumulative and cumulative) based on induced seismicity recorded using a dense seismograph array in the AOI (purple dots). The estimated *b*-value of 1.16, based on an inferred magnitude of completeness of –0.5 M_W, is indicative of likely fault activation during hydraulic-fracturing operations.

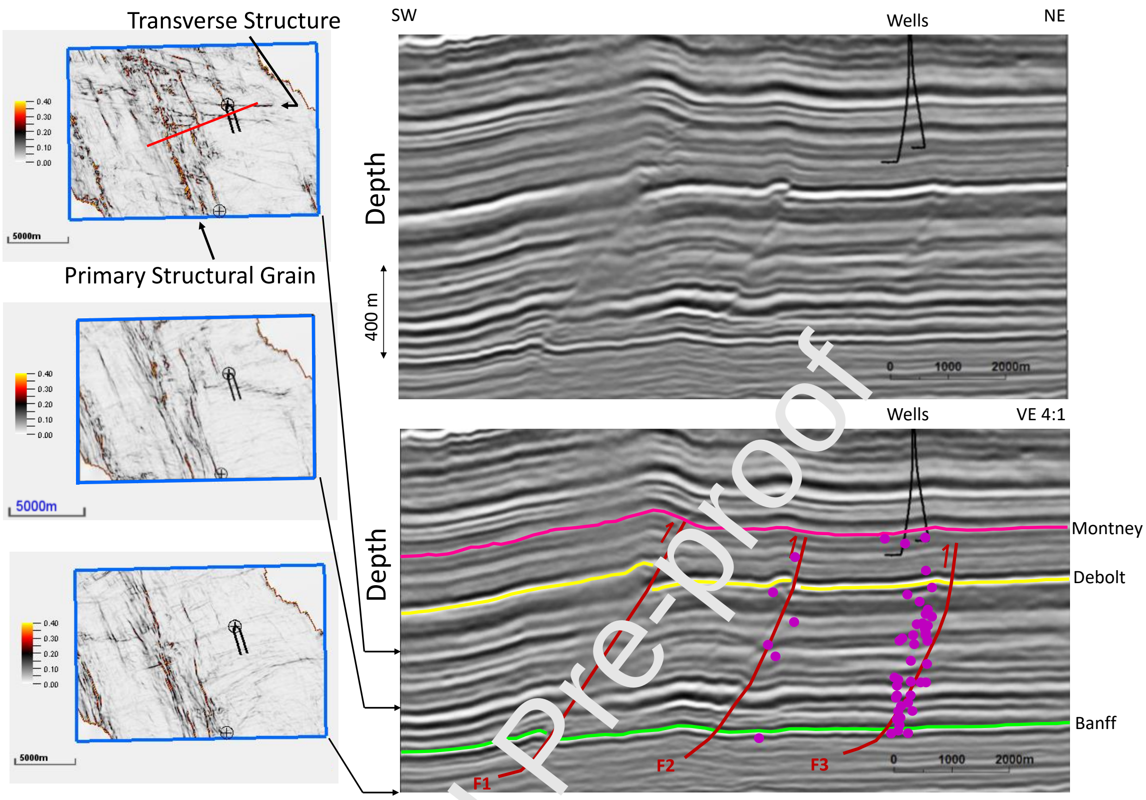

Fig. 2. Images extracted from 3-D seismic data cube. Right panels show uninterpreted (top) and interpreted (lower) ~11-km seismic profile (location shown in top-left panel). F1, F2, F3 are thrust ramps that terminate upwards into anticlines. Magenta dots show hypocenters of induced seismic events projected into the plane of the profile. These events occur mainly within massive carbonates of the Debolt Formation and correlate approximately with faults F2 and F3. Left panels show depth slices (depths are indicated by the arrows at the edge of the profile) depicting variance, a seismic attribute that accentuates reflection discontinuities based on local statistical variance calculated using the seismic data. The location of the profile on the right is shown by a red line and the two wells are shown as black lines. The N15^{o}W primary structural grain is parallel to the strike of the reverse faults. Transverse structures appear as quasi-linear features in the depth sections (left panels) and strike at a high angle to the primary structural grain.

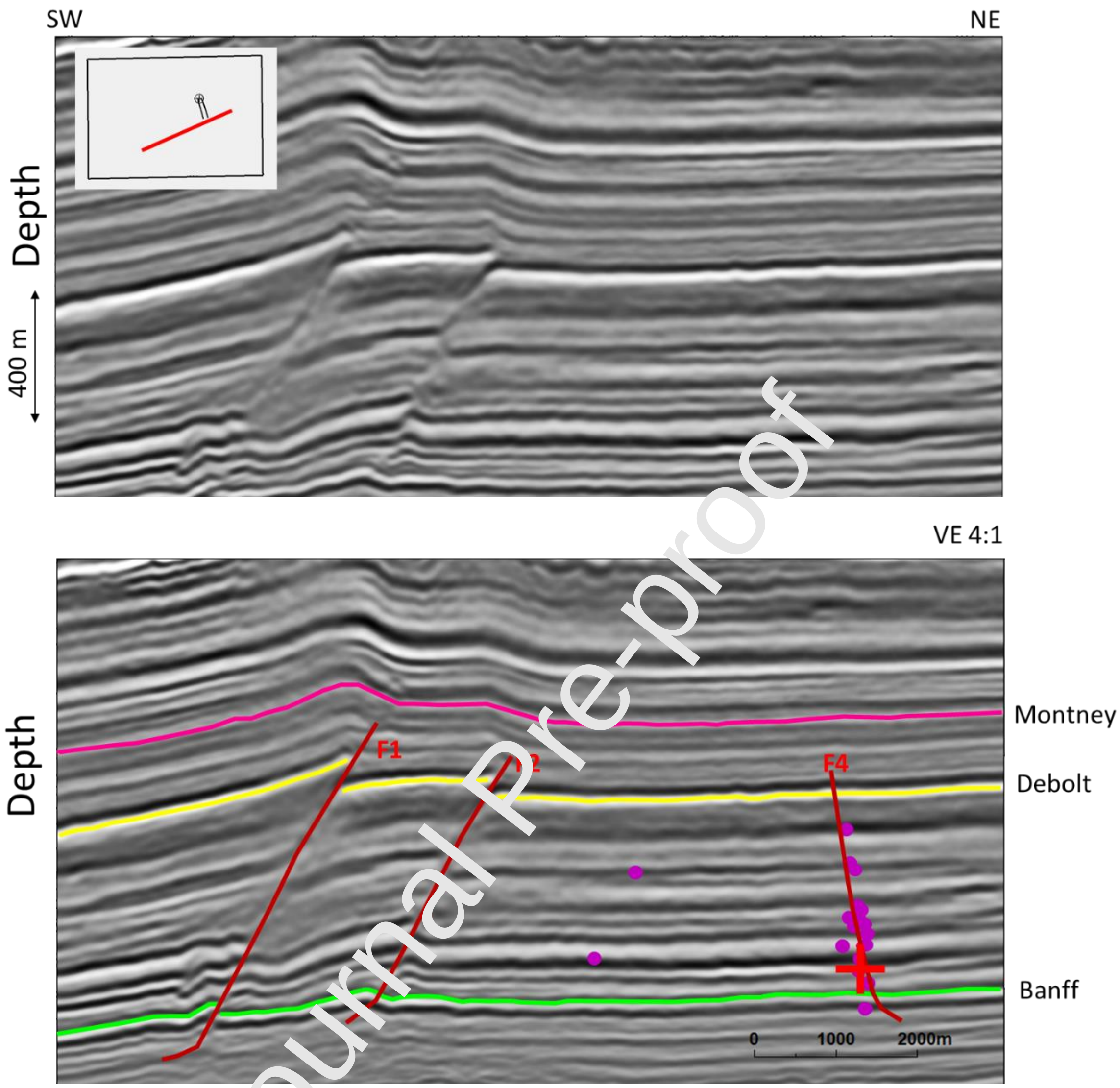

Fig. 3. Seismic imaging of a back-thrust (F4), aided by induced events that occurred about 1.5 km east of the horizontal wells. F1 and F2 are thrust faults that were interpreted using conventional seismic interpretation. Red + symbol shows the location of mainshock (Mw=1.78). The inset shows the location of the seismic section in the AOI.

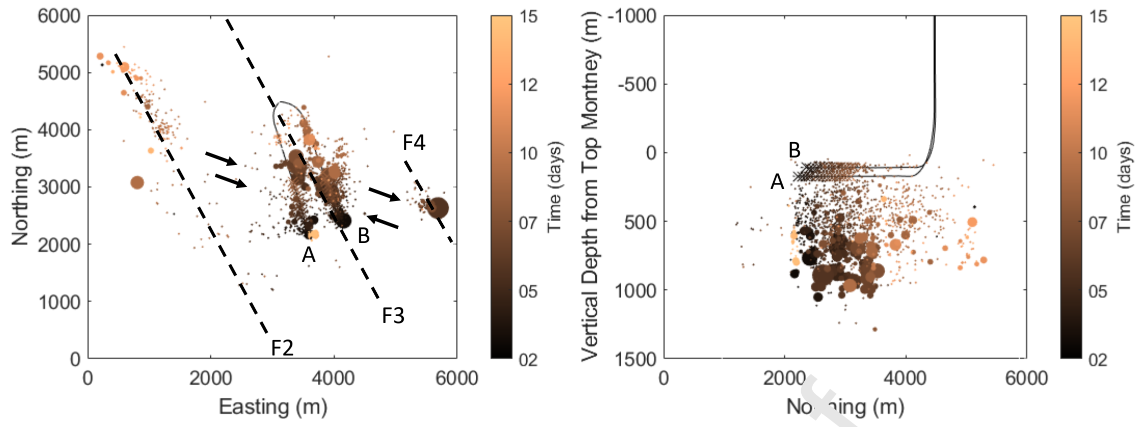

Fig. 4. Location of induced events in map-view (left) and cross section (right) during hydraulic fracturing of Wells A and B. Events are colored by time of occurrence and sized according to magnitude. Stage locations along wells A and B are shown with × symbols. Locations of thrust ramps in the upper Debolt are shown by dashed lines. Arrows indicate interpreted alignment of microseismicity with a transverse structure (Fig. 2) that connects faults F2-F3-F4.

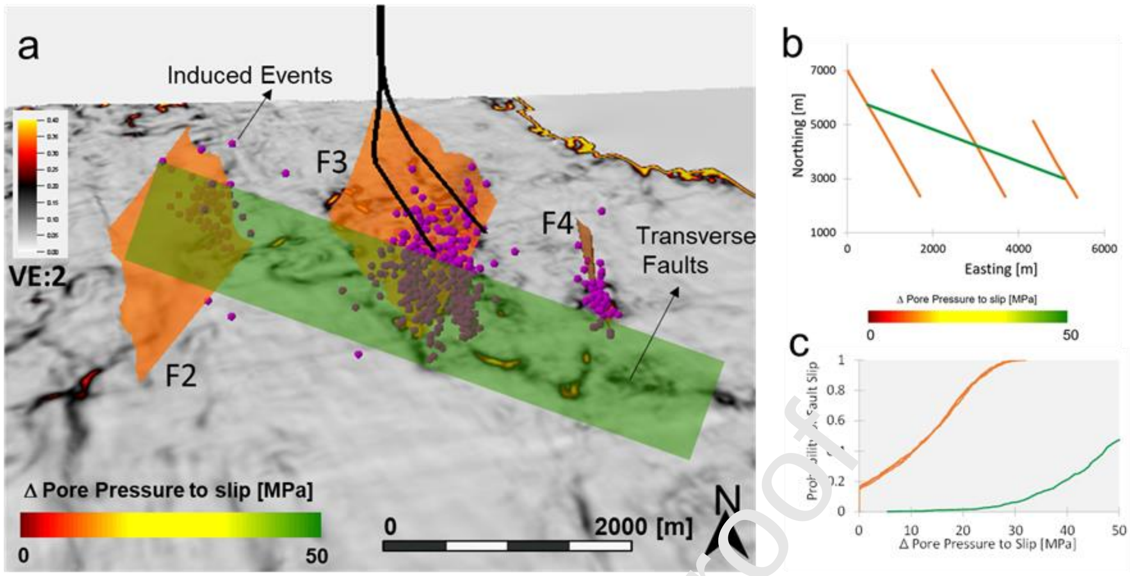

Fig. 5. Summary of fault-slip potential analysis showing 3-D view of interpreted faults adjacent to wells A and B. The variance depth map is also intersected with the fault interpretation with shows the three thrust faults and transverse fault. Faults are colored according to the increase in pore pressure required to bring the fault to failure based on the Mohr-Coulomb criterion with friction μ = 0.6. b shows the plane-view of faults and c is the cumulative distribution function (CDF) of the pore pressure to slip curve for each fault.

Author Contributions

Naimeh Riazi performed the data analysis and figure preparation. Both authors collaborated in project conceptualization and writing the manuscript.

Declaration of interests

☒ The authors declare that they have no known competing financial interests or personal relationships that could have appeared to influence the work reported in this paper.

☐The authors declare the following financial interests/personal relationships which may be considered as potential competing interests:

Highlights

- High-resolution 3-D seismic data provides detailed imaging of a buried thrust system.
- Induced seismic events are accurately located using a novel method.
- Induced seismicity occurred above Precambrian basement.
- Imaged thrust ramps are connected by transverse structures.
- Transverse structures enable inter-fault pore-pressure communication (> 2 km).